Agricultural and Forest Meteorology 382 (2026) 111122

Contents lists available at ScienceDirect

Agricultural and Forest Meteorology

journal homepage: www.elsevier.com/locate/agrformet

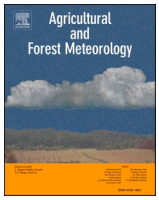

Disentangling the effects of FPAR, CO_2, and climate on terrestrial vegetation productivity trends over two decades (2001–2023)

Jiabin Pu [a,*], Si Gao [b], Kai Yan [b,*], Xian Sun [c], Alexander J. Winkler [d], Qiao Wang [b], Ranga B. Myneni [a]

[a] Department of Earth and Environment, Boston University, Boston, MA 02215, USA
[b] State Key Laboratory of Remote Sensing and Digital Earth, Advanced Interdisciplinary Institute of Satellite Applications, Faculty of Geographical Science, Beijing Normal University, Beijing 100875, China
[c] Aerospace Information Research Institute, Chinese Academy of Sciences, Beijing 100094, China
[d] Max Planck Institute for Biogeochemistry, Jena 07745, Germany

ARTICLE INFO

Keywords:
Gross primary production (GPP)
CO_2 fertilization effect (CFE)
Climate change
FPAR effect

ABSTRACT

Since the early 2000s, human activities have dramatically impacted Earth's environment, leading to significant rising atmospheric CO_2 concentrations and more frequent extreme weather events. Gross primary productivity (GPP), the total carbon fixed by plants via photosynthesis, serves as crucial role for mediating these environmental shifts. This study untangles the effects of CO_2 concentration, climate and canopy structure on GPP. We conceptualized canopy photosynthesis at a location and time instant as dependent on variables that drive photosynthesis in the leaf (CO_2, incident radiation levels, temperature, precipitation and VPD, the latter four denoted as "climate") and the display of leaf area in a canopy, i.e., canopy structure. This structure represents an integration of antecedent effects of CO_2 levels, climate and human activities. These legacy effects are captured by the fraction of photosynthetically active radiation (FPAR) effect in our study. The analysis of global GPP dynamics reveals a substantial increase of nearly 10 Pg C yr^{-1} over the past two decades. Through scenario simulations, this rise was primarily attributed to increasing atmospheric CO_2 concentration, with secondary contributions from the FPAR effect. In contrast, climate change, including warming, droughts, and extreme events, acted as a negative force, somewhat suppressing GPP gains. Furthermore, divergent trends in GPP production amongst biome types highlight the contribution of sparse ecosystems (e.g., grasslands, croplands) to the global GPP increase. Regionally, intensive human land-use practices have amplified GPP growth through significant positive FPAR effect, especially in China and India. Afforestation in China and agricultural intensification in India have led to GPP growth rates exceeding global averages, highlighting the direct role of anthropogenic interventions. In the Amazon region, droughts and climate variability, were the main drivers of GPP fluctuations, but the FPAR effect dominates vegetation carbon fixation divergence across this region due to the light limitation effect for high productivity ecosystems.

1. Introduction

Since the early 1980s, atmospheric CO_2 concentrations have surged from 340 to 430 ppm, driven predominantly by anthropogenic fossil fuel combustion, while global population and economic activity have expanded exponentially (Friedlingstein et al., 2023). These phenomena have catalyzed profound alterations to Earth systems, including direct human activities such as afforestation and agricultural expansion, as well as indirect biogeochemical feedback linked to CO_2 fertilization and biophysical radiative forcing (Nemani et al., 2003; Ballantyne et al., 2017; Chen et al., 2019b; Smith et al., 2020; Song et al., 2022). Central to understanding the sustainability of these trends is the role of vegetation in the global carbon cycle, particularly through photosynthetic carbon assimilation (Cai and Prentice, 2020; Prentice et al., 2024). Gross primary productivity (GPP), representing the total carbon fixed by plants via photosynthesis, constitutes the largest flux in this cycle and serves as a key buffer against anthropogenic CO_2 emissions (Wang et al., 2017; Sha et al., 2022). However, the mechanisms driving long-term

* Corresponding authors.
E-mail addresses: om7759@bu.edu (J. Pu), kaiyan@bnu.edu.cn (K. Yan).

https://doi.org/10.1016/j.agrformet.2026.111122
Received 7 October 2025; Received in revised form 11 December 2025; Accepted 8 March 2026

trends in GPP remain complex, entangled with dynamic interactions between human activities, climatic shifts, and biogeochemical processes.

Long-term satellite observations confirm an extraordinary greening of the land surface (Myneni et al., 1997; Zhu et al., 2016; Piao et al., 2020), particularly evident in China and India (Chen et al., 2019a; Park et al., 2023; Cheng et al., 2024). This greening has undoubtedly led to increased GPP, as has the direct positive CO_2 fertilization effect (CFE), which enhances photosynthetic rates, reduces stomatal conductance and increases water use efficiency (Chen et al., 2022; Ruehr et al., 2023). However, the indirect CO_2 effects, warming and decreased precipitation, coupled with frequent droughts in tropical regions, are deteriorating conditions for GPP in the most productive ecosystems (Huang et al., 2019; Nemani et al., 2003; O'Sullivan et al., 2020; Yang et al., 2023; Zong et al., 2024). And, so did the deforestation, especially in Amazonia and Oceania (Krause et al., 2022). Additionally, mounting evidence indicated that the positive direct CO_2 effects are shifting to negative indirect effects (Chen et al., 2024b). In summary, while anthropogenic greening and CFE have sustained a net increase in GPP over recent decades (Wang et al., 2020; Chen et al., 2022, 2024a), the escalating impacts of climate change threaten to dominate future trends. Consequently, disentangling the contributions of these factors to GPP trends over the past 20 to 30 years is imperative for resolving uncertainties in the terrestrial carbon sink's resilience under accelerating global change.

Theoretically, canopy photosynthesis at a location and time instant can be conceptualized as dependent on variables that drive photosynthesis in the leaf (CO_2, incident radiation levels, temperature, precipitation and VPD, the latter four denoted as "climate") and the display of leaf area in a canopy, i.e., canopy structure. CO_2 and climate variables directly control the instantaneous leaf-level biochemical processes, e.g., Rubisco activity or RuBP regeneration, which can be regarded as the efficiency with which canopy photosynthesis happens, or, the functioning of the photosynthetic system (Knauer et al., 2023; Zhu et al., 2024). The leaf area in a canopy at any location and time can be impacted by various factors (Pei et al., 2022; Sitch et al., 2024), such as human actions (e.g. agriculture, afforestation, silviculture, …) and antecedent (historical) effects of climate (radiation, temperature, precipitation, VPD and soil moisture) change and CO_2 fertilization (Chen et al., 2019b; Smith et al., 2020; Song et al., 2022; Winkler et al., 2021). The factors can be captured by fraction of photosynthetically active radiation (FPAR), which reflects the canopy structure. The functioning of the photosynthetic systems can be mainly impacted by factors such as the instantaneous effect of climate and CO_2 concentration. While stand age, irrigation, and soil nutrient supply (N and P) also influence efficiency, these complex factors are excluded from the modeling framework of this study. Thus, the photosynthetic reaction can be untangled to the effects of CO_2 concentration, climate and canopy structure.

A variety of methods, including statistical methods, process-based land surface models (LSMs), and machine learning (ML) methods, etc., have been widely employed to disentangle the impacts of above factors on vegetation dynamics (Chen et al., 2024a; Sitch et al., 2024; Zhang et al., 2025). Statistical methods, such as principal component analysis (Yao et al., 2018) and correlation indices (Liu et al., 2015), were often used to distinguish the contributions of environmental factors as well as human activities at different spatial scales. Similarly, studies using LSMs with improved plant-water relationship parameterization (Sitch et al., 2024) have quantified the contributions of climate change and global CO_2 to the greening trend in drylands (Jian et al., 2023; Li et al., 2025), while also highlighting the role of human land use (Park et al., 2023). Furthermore, given that ML-based models may not adequately explain CFE, recent efforts propose integrating ML with theoretical photosynthesis models to decouple and evaluate the direct and indirect impacts of multiple environmental factors (Chen et al., 2024a). However, most of these studies primarily focus on individual climate factors, often ignoring the contribution of FPAR effect in photosynthesis. To address this gap, this study adopts TRENDY-like protocols to quantify the drivers of GPP variability (Sitch et al., 2024). Specifically, this study will integrate three production efficiency models (PEMs) driven by two independent climate reanalysis datasets, explicitly isolating FPAR, climate, and CO_2 effects through factorial scenario design. This methodological design to equally quantify contributions from CO_2, climate, and FPAR effects of the photosynthetic process.

2. Materials and methods

2.1. Data source

This study utilized three types of publicly available data (Table 1) for different purposes: (1) input data to drive the PEMs, (2) validation data to assess PEM GPP accuracy, and (3) analysis data for GPP variations.

Two reanalysis climate datasets, GMAO MERRA-2 and ECMWF ERA-5, were used to force the PEMs. Key variables such as air temperature, dew point temperature, and incoming shortwave radiation were extracted. Vapor pressure deficit (VPD) was subsequently calculated from air temperature and dew point temperature (Buck, 1981). Additional climate data (net radiation, evapotranspiration, and precipitation), required by PEM3, were obtained from GLDAS NOAH-2.1. A crucial PEM input, the FPAR, was acquired from the sensor-independent (SI) FPAR dataset (Pu et al., 2024). Daily CO_2 data from NOAA were used to model the CFE (Lobell and Field, 2008). All climate and SI FPAR data were harmonized to daily and 0.05° resolutions for GPP calculation with the three PEMs. The study addresses the temporal and spatial resolution challenges of climatic inputs through specific data processing steps. To accurately reflect photosynthetic activity, which is confined to daylight hours, this study employs diurnal climate data (e.g., hourly temperature and VPD) instead of standard daily aggregates. Daylight hours are specifically defined as periods where hourly downward shortwave radiation exceeds zero. Variables such as the mean or minimum temperature during these periods are then derived for input into the three PEMs. A significant challenge addressed is the mismatch in spatial resolution between the coarse-resolution meteorological data (C1/C2) and the target resolution of 0.05° To enhance the meteorological inputs, spatial interpolation is utilized. This involves identifying the four nearest coarse-resolution pixels from the C1/C2 datasets to a given 0.05° target pixel and applying the cosine interpolation algorithm adopted from the MODIS GPP program (Running and Zhao, 2015) for weighted averaging.

Model parameters were optimized through constrained calibration using FLUXNET2015 data (Pastorello et al., 2020) to enhance simulation accuracy. These PEM parameters are land cover dependent (Sulla-Menashe and Friedl, 2018), with the MODIS land cover product used to identify the land cover for each pixel. Following the UMD classification scheme (LC_Type_2) of the MODIS MCD12Q1 product, vegetation was aggregated into 11 biomes: evergreen needleleaf forest (ENF), evergreen broadleaf forest (EBF), deciduous needleleaf forest (DNF), deciduous broadleaf forest (DBF), mixed forest (MF), closed shrubland (CSH), open shrubland (OSH), wooded savanna (WSA), savanna (SAV), grassland (GRA), and cropland (CRO).

AmeriFlux (Novick et al., 2018), an independent dataset from FLUXNET2015, provided in-situ GPP for validation and accuracy assessment. The Orbiting Carbon Observatory-2 Solar-Induced Fluorescence (SIF) product (GOSIF) GPP, derived from biome-specific relationships between reconstructed SIF (based on discrete OCO-2 SIF soundings, remote sensing data from the MODIS, and meteorological reanalysis data) and tower GPP, which exhibits similar spatiotemporal patterns to PEM and provides different insights to global carbon cycle via observation-based estimates, served as a reference for evaluation. Furthermore, the minimum water level of the Negro River was used to indicate drought conditions in the Amazon forests. The Multivariate ENSO Index from NOAA, illustrating the occurrence of ENSO events since the 1980s, was used to assess the correlation between El Niño

Table 1
Variables used in this study and their attributes.

Use	Dataset provider	Variable	Temporal coverage	Spatial resolution	Temporal resolution	Source
Input for PEM	GMAO MERRA-2	Air temperature; Dew point temperature; Incoming shortwave radiation	1980 - present	0.5°lat/ 0.625°lon	3 h	https://gmao.gsfc.nasa.gov/reanalysis/MERRA-2
	ECMWF ERA-5	Air temperature; Dew point temperature; Incoming shortwave radiation	1950 - present	0.1°	Monthly	https://cds.climate.copernicus.eu/cdsapp#!/dataset/reanalysis-era5-single-levels
	GLDAS NOAH-2.1	Net Radiation; Evapotranspiration; Precipitation	2000 - present	0.25°	3 h	https://disc.gsfc.nasa.gov/datasets?keywords=GLDAS
	NOAA CO_2 concentration	CO_2	1958 - present	-	Daily	https://gml.noaa.gov/ccgg/trends/
	MODIS Landcover	Landcover	2001 - 2020	500m	Annual	https://lpdaac.usgs.gov/products/mcd12q1v061/
	SI FPAR CDR	FPAR	2000 - present	500m	8d	https://doi.org/10.5281/zenodo.8076540
	FluxNet2015	In-situ GPP for optimization	1990 - 2014	-	Half hour	https://fluxnet.org/data/fluxnet2015-dataset/
Evaluation data of PEM	AmeriFlux	In-situ GPP for validation	2000 - 2001	-	Half hour	https://ameriflux.lbl.gov/data/download-data/
	GOSIF	Global GPP for comparison	2000 - present	0.05°	8d	https://data.globalecology.unh.edu/data/GOSIF_v2/
Analysis data	minimum water level negro river	Drought indicator in Amazon	2000 - present	-	daily	https://www.portodemanaus.com.br/?pagina=niveis-maximo-minimo-do-rio-negro
	El Niño events	El Niño intensities	1979 - present	-	monthly	https://psl.noaa.gov/enso/mei/

intensities and GPP in tropical regions.

2.2. Production efficiency model (PEM)

The PEM GPP constitutes an ensemble average derived from three PEMs (detailed below) and two independent climate datasets. The three PEMs include: (1) the modified MOD17 algorithm incorporating the CFE (PEM1), (2) the EC-LUE model (PEM2), and (3) the MPI-Jena biochemical model (PEM3). These models were driven by key environmental drivers including biome-specific parameters, FPAR, incident PAR, temperature, CO_2 concentration, VPD, and soil moisture (Keenan et al., 2023; Running and Zhao, 2015; Yuan et al., 2007; Zheng et al., 2020; Bao et al., 2022, 2023).

2.2.1. PEM1: MOD17 with CFE

The PEM1 used for generating GPP by the MODIS program is modified to include the CFE (Keenan et al., 2023). GPP (g C m^{-2} $_D$$^{-1}$) is calculated as follows:

$$GPP_{M1} = LUE_{opt}^{M1} \times PAR \times FPAR \times f_{TMIN}^{M1} \times f_{VPD}^{M1} \times f(CO_2) \quad (1)$$

$$f_{TMIN}^{M1} = \begin{cases} 0, TMIN \le TMIN_{min} \\ \dfrac{TMIN - TMIN_{min}}{TMIN_{max} - TMIN_{min}}, TMIN_{min} < TMIN < TMIN_{max} \\ 1, TMIN \ge TMIN_{max} \end{cases} \quad (2)$$

$$f_{VPD}^{M1} = \begin{cases} 0, VPD \ge VPD_{max} \\ \dfrac{VPD_{max} - VPD}{VPD_{max} - VPD_{min}}, VPD_{min} < VPD < VPD_{max} \\ 1, VPD \le VPD_{min} \end{cases} \quad (3)$$

$$f(CO_2) = \frac{C_s^t}{C_s^{base}} \quad (4)$$

where, LUE_{opt}^{M1} is the optimal light use efficiency (g C MJ^{-1}) for three PEM1; PAR is the incident photosynthetically active radiation (MJ m^{-2} day^{-1}); FPAR is the fraction of vegetation absorbed PAR (Knyazikhin et al., 1998); f_{TMIN}^{M1} (Eq. (2)) and f_{VPD}^{M1} (Eq. (3)) are the temperature (daily minimum) and water stress scalar for PEM1, where VPD_{max}, VPD_{min}, $TMIN_{min}$, and $TMIN_{max}$ are the parameters dependent on vegetation types (Running and Zhao, 2015); $f(CO_2)$ is the effect of atmospheric CO_2 concentration on PEM1 GPP (Keenan et al., 2023), which is the relative value of current year C_s (the CFE for PEM2, Eq. (5)) compared to year 2001.

$$C_s = \frac{C_i - \Gamma^*}{C_i + 2\Gamma^*} \quad (5)$$

$$C_i = C_a \times \chi \quad (6)$$

where C_s is the effect of atmospheric CO_2 concentration, VPD, and temperature on GPP; Γ^* is the CO_2 compensation point in the absence of dark respiration (ppm) and C_i is the CO_2 concentration in the intercellular air spaces of the leaf (ppm), which is the product of the atmospheric CO_2 concentration (Ca) and the ratio of internal to ambient CO_2 in the leaf (χ) (Farquhar et al., 1980; Prentice et al., 2014; Keenan et al., 2016). χ is calculated by

$$\chi = \frac{\varepsilon}{\varepsilon + \sqrt{VPD}} \quad (7)$$

$$\varepsilon = \sqrt{\frac{356.51 \times K}{1.6 \times \eta^*}} \quad (8)$$

$$K = K_c \times \left(1 + \frac{P_o}{K_o}\right) \quad (9)$$

$$K_c = 39.97 \times e^{\frac{79.43 \times (T_a - 298.15)}{298.15 \times R \times T_a}} \quad (10)$$

$$K_o = 27480 \times e^{\frac{36.38 \times (T_a - 298.15)}{298.15 \times R \times T_a}} \quad (11)$$

where K_c (Pa) and K_o (Pa) are the Michaelis-Menten coefficient of Rubisco for carboxylation and oxygenation, respectively (Keenan et al., 2016); P_o is the partial pressure of O_2 (Pa) and R is the molar gas constant (8.314 J mol^{-1} K^{-1}) (Keenan et al., 2016); η^* is the viscosity of water as a function of air temperature relative to its value at 25 °C (Korson et al., 1969).

2.2.2. PEM2: EC-LUE

The PEM2 (EC-LUE model) was proposed by Yuan et al. (2007) and this model calculates GPP as follows:

$$GPP_{M2} = LUE_{opt}^{M2} \times PAR \times FPAR \times \min\left(f_T^{M2}, f_{VPD}^{M2}\right) \times C_s \quad (12)$$

$$f_T^{M2} = \frac{(T - T_{max}) \times (T - T_{min})}{(T - T_{max}) \times (T - T_{min}) - (T - T_{opt})^2} \quad (13)$$

$$f_{VPD}^{M2} = \frac{VPD_0}{VPD + VPD_0} \quad (14)$$

where LUE_{opt}^{M2} is the optimal light use efficiency (g C MJ^{-1}) for PEM2; f_T^{M2} and f_{VPD}^{M2} are the temperature and the water stress scalar for PEM2, where T_{min}, T_{opt}, and T_{max} are the minimum, optimum, and maximum temperatures for vegetation photosynthesis, respectively (Yuan et al., 2007); VPD_0 is the half-saturation coefficient of the VPD constraint equation (kPa); C_s (same as Eq. (5)) is the effect of atmospheric CO_2 concentration, VPD, and temperature.

2.2.3. PEM3: MPI-BGC

The Max Planck Institute for Biogeochemistry (MPI-BGC, PEM3) model evaluates GPP as:

$$GPP_{M3} = LUE_{opt}^{M3} \times PAR \times FPAR \times f_T^{M3} \times f_{VPD,CO2}^{M3} \times f_W^{M3} \times f_L^{M3} \times f_{CI}^{M3} \quad (15)$$

where LUE_{opt}^{M3} is the optimal light use efficiency (g C MJ^{-1}) for PEM3; f_T^{M3} is the temperature stress scalar for PEM3 and $f_{VPD,CO2}^{M3}$ is the water stress scalar that consider CFE for PEM3 (Kalliokoski et al., 2018); f_W^{M3}, f_L^{M3}, and f_{CI}^{M3} are the effects of soil moisture (W, which is estimated by water availability index using precipitation and evapotranspiration), light intensity (L), and cloudiness index (CI) on GPP, respectively.

$$f_T^{M3} = \frac{2e^{-\left(T_f - T_{opt}\right)/k_T}}{1 + e^{\left(-\left(T_f - T_{opt}\right)/k_T\right)^2}} \quad (16)$$

$$T_f(t) = (1 - \alpha_T) \times T(t) + \alpha_T \times T(t-1) \quad (17)$$

where T_{opt}, k_T, α_T are optimal temperature, sensitivity to temperature dynamics, and lag parameter for temperature effect, respectively (Horn and Schulz, 2011).

$$f_{VPD,CO2}^{M3} = \left(e^{k \times \left(\frac{C_{a0}}{C_a}\right)^{C_k} \times VPD}\right) \times \left(1 + \frac{C_a - C_{a0}}{C_a - C_{a0} + c_m}\right) \quad (18)$$

where k is the sensitivity to VPD changes (Mäkelä et al., 2008); C_{a0} is the minimum optimal atmospheric CO_2 concentration; Ca is the atmospheric CO_2 concentration; C_k is the sensitivity to atmospheric CO_2 concentration changes; and c_m is the CO_2 fertilization intensity indicator (Kalliokoski et al., 2018).

$$f_W^{M3} = \frac{1}{1 + e^{k_W \times (W_f - W_I)}} \quad (19)$$

$$W_f(t) = (1 - \alpha_W) \times W(t) + \alpha_W \times W(t-1) \quad (20)$$

where k_W, W_I, and α_W are sensitivity to soil moisture changes, optimal soil moisture, and lag parameter for soil moisture effect (Horn and Schulz, 2011).

$$f_L^{M3} = \frac{1}{1 + \gamma \times PAR \times FPAR} \quad (21)$$

where γ is light saturation curvature indicator (Mäkelä et al., 2008).

$$f_{CI}^{M3} = CI^{\mu} \quad (22)$$

where μ is sensitivity to cloudiness index changes (Bao et al., 2022).

2.2.4. Estimation of optimal LUEs

Optimal values of light use efficiency (LUE_{opt}) for the 11 land covers (detailed in Section 2.1) are estimated iteratively and separately for the three PEMs using annual GPP estimates derived from the FLUXNET2015 dataset (averaging night-time (GPP_REF_NT_VUT) and day-time (GPP_REF_DT_VUT) partitioning approaches). Carbon flux data of 189 sites from the FLUXNET2015 dataset were selected (detailed in Table S1) for optimization. The number of GPP estimates for each land cover varies depending on the number of sites belonging to that land cover and the number of years for which estimates are available (total 1410 site years). For each land cover type, the optimization involved four steps: (1) Simulating GPP for half of the randomly selected observations by assuming LUE = 1 with GMAO meteorological data and SI FPAR inputs; (2) Estimating a preliminary LUE_{opt} via linear regression between simulated and observed GPP; (3) Applying this LUE_{opt} to model GPP for the remaining half of the data; (4) Calculating the RMSE by regressing the modelled GPP values in Step 3 against the corresponding observed GPP values. Steps 1 to 4 are repeated 10,000 times to obtain 10,000 values of LUE_{opt} and corresponding RMSE and the final LUE_{opt} (Table S2) was determined by averaging the top 9500 results with the lowest RMSE. The detailed results of PEM GPP after optimization (Fig. S1) can be found in Appendix A1.

2.2.5. Evaluation

This study utilizes observation-derived and model-simulated GPP data spanning 2001 to 2023 to represent long-term satellite-based GPP products. The modeled PEM GPP will be evaluated for its accuracy at a local scale through comparison with independent AmeriFlux estimates (Novick et al., 2018). These validation sites (142 sites, totaling 910 site-years; Table S3) are distinct from the FLUXNET2015 estimates used to optimize the LUE variable of the three PEMs. First, the accuracy of the temporal GPP will be assessed by the correlation coefficient (R) and Root Mean Square Error (RMSE) per site (Table S3). Second, the temporospatial variability of mean GPP will be validated against GPP_{obs} across all sites (Fig. S2). The accuracy asscessment of PEM GPP can be found in Appendix A2.

The observational benchmark integrates solar-induced chlorophyll fluorescence (SIF) data from the Orbiting Carbon Observatory-2 (GOSIF) with eddy covariance flux tower measurements, forming the GOSIF GPP product (Li and Xiao, 2019). This hybrid dataset, generated through the empirical scaling of satellite SIF observations using tower-based GPP constraints, will be used to compare consistency with the modeled PEM GPP (Figs. S3 and S4). This study will not only compare the spatial and temporal patterns of GOSIF and PEM GPPs (details can be found in Appendix A2) but also conduct a comprehensive trend analysis between these two GPP products to confirm the accuracy of the PEM GPP analysis.

2.3. Analysis of driving mechanism

The spatial-temporal patterns of GPP are primarily governed by anthropogenic activities, operating through two temporal pathways: (1) current effects involving direct land cover alterations (cropland expansion, afforestation, deforestation) and indirect climate modulation via CO_2-induced radiative forcing (impacting radiation, temperature, precipitation, VPD, and soil moisture), alongside increased disturbance frequencies (wildfires, pests); (2) legacy effects arising from historical environmental modifications that induce delayed photosynthetic responses. Mechanistically, these drivers regulate GPP through biochemical constraints, current CO_2 levels and microclimate jointly control Rubisco activity (light-saturated conditions) or RuBP regeneration

(light-limited conditions) at the leaf scale, and through canopy structural feedbacks, where cumulative GPP alters leaf area index (LAI) and induces FPAR saturation effects through iterative canopy-light interactions (Thornley, 2002; Gao et al., 2023; Stocker et al., 2020). In summary, as shown in the Fig. 1a, CO_2 and Climate (incident radiation, temperature, VPD, and precipitation) directly control the leaf-level biochemical processes at a location and time instant. While FPAR reflects canopy structure, i.e. the display of leaf area. This structure is the result of various factors, including antecedent CO_2 levels, historical climate and human activities affecting vegetation growth.

Although advanced dynamic models (TRENDY DGVMs, CMIP6 ESMs) partially incorporate these linkages (Gier et al., 2024; Sitch et al., 2024), their application is constrained by persistent biases in simulating GPP magnitude and seasonal trajectories across global ecosystems (Westermann et al., 2024). PEMs combines data measurability (CO_2, climate, and FPAR) with structural simplicity. This model captures the direct effects of these variables on primary productivity, enabling sensitivity simulations to achieve the primary objective of understanding the spatial patterns observed in GPP. Thus, this study analyzed the drivers of global GPP using an ensemble of three PEMs driven by two climate datasets.

Our methodology advances through three sensitivity experiments adopting TRENDY protocols (Fig. 1b). The CFE is quantified through simulation S1 by using constant climate (2001–2003 average), FPAR, and landcover from year 2001 and time-varying observed CO_2 concentration for the period 2001–2023. The climate effect is quantified as the difference between simulations S2 and S1, where S2 is performed with FPAR and landcover from year 2001 and time-varying observed CO_2 concentration and climate for the period 2001–2023. Finally, the effect of FPAR is quantified as the difference between simulations S3 and S2, where S3 is performed with time-varying observed CO_2 concentration, climate, FPAR and landcover for the period 2001–2023. Notably, land cover information in S3 changes only in conjunction with FPAR; thus, the FPAR effect implicitly incorporates land use/land cover changes. This synthesis of observationally constrained PEMs with factorial parameterization enables precise discrimination between biophysical responses to atmospheric changes and direct human landscape alterations, overcoming systemic biases in process-based model simulations.

2.4. Trend analysis

Trends in annual average GPPs (2001 to 2023) are evaluated by the Mann–Kendall (MK) test. The MK test is a non-parametric statistical test commonly used for climate diagnostics and prediction. It enables the detection of monotonic trends in time series data, helping to determine if significant trends exist (Hamed and Rao, 1998). The MK test is employed as follows:

$$S = \sum_{i=1}^{n-1} \sum_{j=i+1}^{n} \mathrm{sgn}(x_j - x_i) \tag{23}$$

$$\mathrm{Var}(S) = \frac{n(n-1)(2n+5) - \sum_{i=1}^{m} t_i(t_i-1)(2t_i+5)}{18} \tag{24}$$

$$Z_s = \begin{cases} \dfrac{S-1}{\sqrt{\mathrm{Var}(S)}}, & if\ S > 0 \\ 0, & if\ S = 0 \\ \dfrac{S+1}{\sqrt{\mathrm{Var}(S)}}, & if\ S < 0 \end{cases} \tag{25}$$

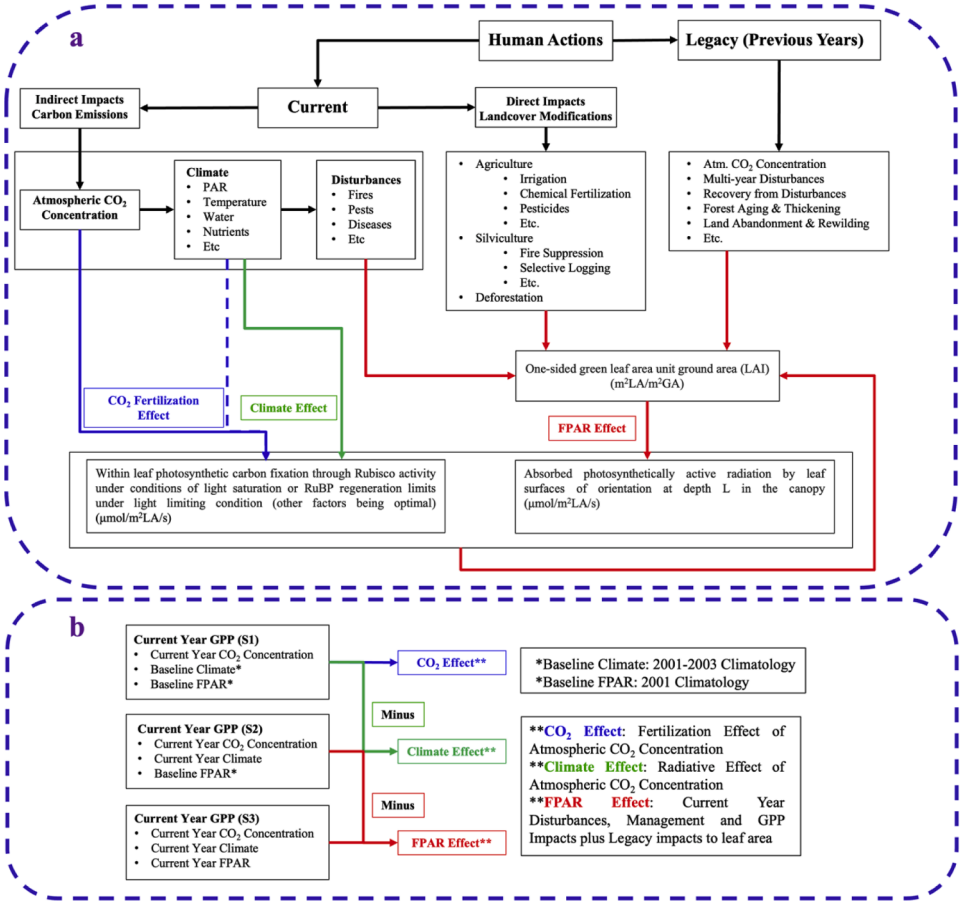

Fig. 1. Schematic diagram of understanding of drivers of photosynthetic production (a) and simulation experiments designed (b).

Eq. (23) calculates the sum (S) of step function values, which represent the differences between values at different points (x_j and x_i) in the time series. The variables n and m denote the number of data points and the number of tied groups (recurring data sets), respectively. Next in Eq. (24), the variance (Var(S)) is calculated by assessing the magnitude of S to evaluate the statistical significance of the detected trends. Where the t_i is the number of the ties (the number of repeats in the extent i). Finally, we calculated the test statistic Z_s (Eq. (25)). When $|Z_s| > Z_{1-\alpha/2}$, the null hypothesis (i.e., no trend) is rejected and the α is a special significance level. Here, we use the significance level of $\alpha = 0.1$ and the $Z_{1-\alpha/2} = 1.28$. Thus, the trends with $P \leq 0.1$ are statistically significant in this paper.

3. Results

3.1. Globally increasing GPP includes the respective contributions of climate, CO_2 and FPAR

The annual mean of global GPP from PEMs was comparable to the GOSIF estimate (129.5 vs. 132.7 Pg C yr^{-1}) across the vegetated area, averaged from 2001 to 2023. Both PEM and GOSIF GPPs showed a consistent upward trend of 4.5 ~ 4.6 Pg C yr^{-1} $decade^{-1}$ during this period. Geographically, GPP trends over the past two to three decades displayed prominent increases in China and India, while declines were observed in the tropical belt, especially in Amazonia (Figs. 2 and S5). Statistically, approximately 42.8 % to 46.0 % of the total vegetated area exhibited an upward trend, most significant in East Asia, Europe, India, North America, the Sahel and surrounding areas, and northern Siberia. Declines were observed in only 6.2 % to 6.3 % of vegetated lands for PEM GPP, notably concentrated in the Brazilian Amazon (though more scattered in GOSIF). Additionally, GPP distribution trends revealed a substantial increase in the GPP of sparse vegetation, primarily shrublands and grasslands, in arid and semi-arid regions.

Dissecting the trends presented in Fig. 2, Fig. S5, and Fig. 3, climate change had a small and statistically insignificant negative effect on GPP (−0.4 Pg C yr^{-1} $decade^{-1}$), whereas FPAR effect and CFE exerted significant positive impacts (1.5 and 3.5 Pg C yr^{-1} $decade^{-1}$). All three drivers combined resulted in a net positive effect of 4.6 Pg C yr^{-1} $decade^{-1}$. From a spatial perspective, the CFE's influence was relatively uniform globally (Fig. 3c). The Amazon Forest region, however, was predominantly affected by a negative climate effect (Fig. 3a), where the positive FPAR effect was offset by climate-induced declines, leading to an overall GPP reduction. In contrast, the combined influence of CFE and the FPAR effect explained the higher GPP growth rates observed in China, India, and Sub-Saharan Africa compared to other regions. This suggests that the degradation of global vegetation productivity over the past two to three decades due to a deteriorating climate has been largely offset by human-induced land greening, particularly in China and India. Overall, the modelled patterns matched well with observations and previous studies. CO_2 fertilization, climate change, land use/land cover changes were the principal reasons for these GPP changes.

3.2. Divergent trends in GPP production amongst vegetation types

Vegetation exhibited biome-specific responses to the biochemical fertilization effect and radiative effect from increasing CO_2, modulated by distinct canopy structures and leaf properties. Global GPP trends demonstrated pronounced divergence across vegetation types, with net gains predominantly occurring in sparse ecosystems (more than 4 Pg C yr^{-1} $decade^{-1}$ from WSA, SAV, GRA, and CRO. Table 2). Excluding forests (0.5 ~ 0.8 Pg C yr^{-1} $decade^{-1}$), both herbaceous vegetation, croplands, and other woody vegetation showed marked productivity increases (more than 4 % $decade^{-1}$, Figs. 4a and 5). This structural transformation was quantified by rising herbaceous to woody vegetation ratios (1.8 ~ 2.5 % $decade^{-1}$) and other woody vegetation to forests ratios (2.2 ~ 2.4 % $decade^{-1}$) from 2001 to 2023 (Fig. 4b). Meanwhile, the GPP for croplands and the cropland to other herbaceous vegetation ratio increased continuously (7.4 ~ 7.8 % $decade^{-1}$), which reflected agricultural intensification (Fig. 4a). Scenario simulation revealed differential driver dominance, the CFE consistently showed positive effects for all vegetation growth (2.3 ~ 3.7 % $decade^{-1}$), and the CFE coupled with the FPAR effect led to enhanced growth in all vegetation types except forests (Fig. 5). For forests, both the climate effect (−0.9 % $decade^{-1}$) and FPAR effect (−0.9 % $decade^{-1}$) were statistically negative, offsetting the positive CFE (2.3 % $decade^{-1}$) and resulting in only a small enhancement in productivity (0.5 ~ 0.8 % $decade^{-1}$).

Forests generally showed stable dynamics (Fig. 4a) because their high-density canopies can be limited by light distribution, soil moisture, and temperature. This explains why the CFE was counteracted by the negative FPAR effect and climate effect (Fig. 5). Forest GPP dynamics also varied across latitudinal zones. Both temperate and boreal forests exhibited a slightly increasing GPP trend (0.5 Pg C yr^{-1} $decade^{-1}$ and 0.2 Pg C yr^{-1} $decade^{-1}$, Fig. S6a), with a positive climate effect (Fig. S7) indicating that higher temperatures support forest growth (e.g., longer

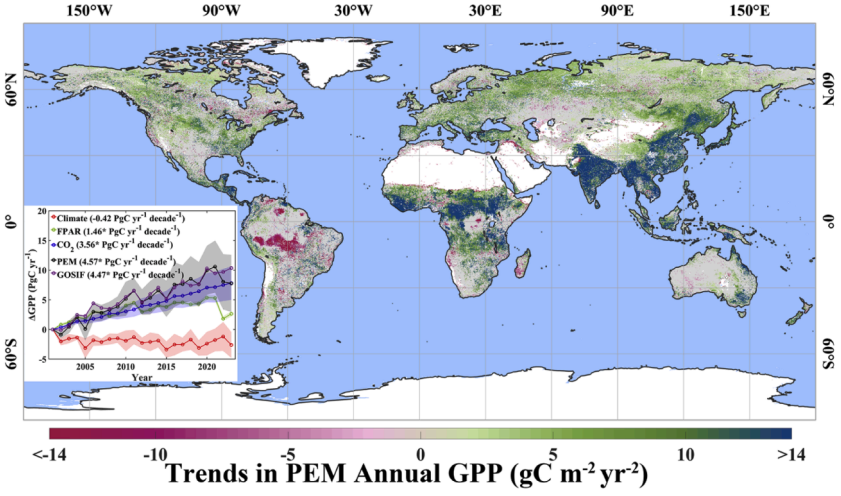

Fig. 2. Spatial patterns of trends in PEM GPP during 2001–2023. Statistically significant trends (Mann–Kendall test, $P \leq 0.1$) are color-coded. Grey areas show vegetated land with statistically insignificant trends. White areas depict barren lands, permanent ice-covered areas, permanent wetlands, and built-up areas. Blue areas represent water. The inset shows global-scale trends from climate effect (6 PEM GPPs, mean as red line and range as red shading), FPAR effect (green), CFE (blue), PEMs (black), and GOSIF (purple, from Fig. S5). '*' means the trend is statistically significant (Mann–Kendall test, $P \leq 0.1$).

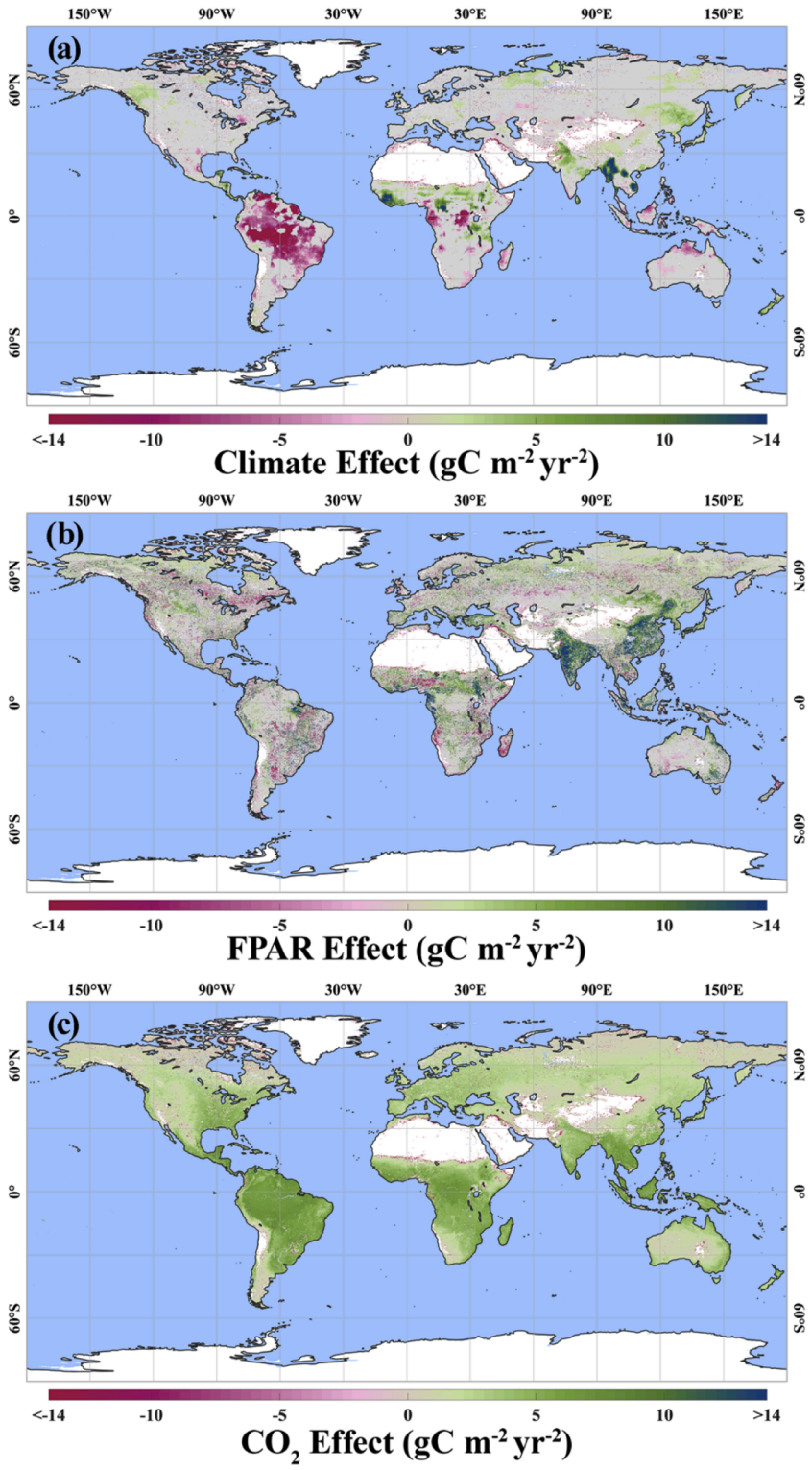

Fig. 3. Spatial patterns of climate effect (a), FPAR effect (b), and CFE (c) on photosynthetic production during 2001–2023. Statistically significant trends (Mann–Kendall test, $P \leq 0.1$) are color-coded. Grey areas show vegetated land with statistically insignificant trends. White areas depict barren lands, permanent ice-covered areas, permanent wetlands, and built-up areas. Blue areas represent water.

phenology seasons) in the mid- and high-latitude Northern Hemisphere. However, these upward trends were offset by declines in tropical forests, particularly in the Amazon ($-0.5 \sim -0.3$ Pg C yr^{-1} $decade^{-1}$, Fig. S6b), where higher temperatures led to drought conditions that limited carbon fixation.

3.3. The outsize contribution of croplands in India and forests in China to global GPP increase

Figs. 6 and S8 illustrate the extensive greening of China & India in the twenty-first century, almost 70.5 ~ 81.2 % of the vegetated areas in these regions exhibited a significant upward trend in GPP, while only 2.8

Table 2
Annual average GPP and trends of different landcovers for PEM and GOSIF. ENF is evergreen needleleaf forest, EBF is evergreen broadleaf forest, DNF is deciduous needleleaf forest, DBF is deciduous broadleaf forest, MF is mixed forest, CSH is closed shrubland, OSH is open shrubland, WSA is wooded savanna, SAV is savanna, GRA is grassland and CRO is cropland. '*' means the trend is statistically significant (Mann–Kendall test, $P \leq 0.1$).

landcover (Area in %)	PEM Annual GPP (Pg C yr^{-1})	GOSIF Annual GPP (Pg C yr^{-1})	PEM Annual GPP Trends (Pg C yr^{-1} dec^{-1})	GOSIF Annual GPP Trends (Pg C yr^{-1} dec^{-1})
Global (100 %)	129.48 ±3.28 (100 %)	132.69 ±3.15 (100 %)	4.57* (3.53 %)	4.47* (3.37 %)
ENF (2.27 %)	3.11±0.08 (2.40 %)	2.25±0.06 (1.69 %)	0.06* (1.87 %)	0.07* (3.12 %)
EBF (11.31 %)	34.85±0.53 (26.92 %)	38.21±0.38 (28.80 %)	−0.42* (−1.22 %)	−0.17 (−0.45 %)
DNF (0.39 %)	0.37±0.03 (0.29 %)	0.32±0.03 (0.24 %)	−0.01 (−1.81 %)	−0.01 (−3.23 %)
DBF (2.72 %)	4.26±0.12 (3.29 %)	5.38±0.10 (4.06 %)	0.14* (3.35 %)	0.11* (2.06 %)
MF (4.51 %)	6.16±0.34 (4.76 %)	5.85±0.30 (4.41 %)	0.48* (7.79 %)	0.43* (7.40 %)
CSH (0.51 %)	0.40±0.03 (0.31 %)	0.42±0.03 (0.32 %)	−0.03* (−7.25 %)	−0.04* (−8.39 %)
OSH (12.49 %)	4.71±0.26 (3.63 %)	4.20±0.24 (3.17 %)	0.20* (4.24 %)	0.21* (4.91 %)
WSA (10.73 %)	15.81±0.78 (12.21 %)	16.86±0.81 (12.71 %)	1.10* (6.99 %)	1.14* (6.74 %)
SAV (15.23 %)	24.43±0.55 (18.87 %)	24.50±0.45 (18.46 %)	0.69* (2.83 %)	0.59* (2.42 %)
GRA (28.83 %)	21.71±0.95 (16.77 %)	21.83±0.87 (16.45 %)	1.29* (5.92 %)	1.18* (5.40 %)
CRO (11.00 %)	13.67±0.76 (10.56 %)	12.87±0.68 (9.70 %)	1.06* (7.79 %)	0.95* (7.42 %)

% to 3.7 % showed a significant negative trend (Figs. 6a and S8a). The growth rate of GPP (Figs, 6b and S8b) in China & India (9.0 ~ 10.9 % $decade^{-1}$) was more than 3 times that of the rest of the world (ROW, 2.7 ~ 3.0 % $decade^{-1}$). The main factor differentiating China & India from the ROW was the human-driven FPAR effect (5.4 % $decade^{-1}$ vs. 0.8 % $decade^{-1}$, Fig. 7). Furthermore, China and India exhibited distinct drivers for their greening, while forests contributed 40.4 ~ 53.4 % to the GPP enhancement in China, whereas croplands alone accounted for 72.5 % to 78.3 % of the increase in India. Focusing on China's forested lands, GPP surged at an alarming rate of 18.4 ~ 21.5 % $decade^{-1}$ (Figs. 6c and S8c), with the FPAR effect contributing nearly 80 % (14.7 % $decade^{-1}$, Fig. 7). This substantial increase was primarily driven by forest area and total leaf area expansion. In contrast, GPP in forests of the ROW (excluding China's forests) did not show significant change (Figs. 6c and S8c). China's ambitious programs to protect and expand its forests, aimed at mitigating soil erosion, air pollution, and climate change, underscore the critical role of human action in the greening of its forest lands. Regarding cropland greening in India, GPP increased at a rate of 13.6 ~ 14.6 % $decade^{-1}$, more than double that of croplands in the ROW (6.1 ~ 6.4 % $decade^{-1}$, Figs. 6c and S8c). The main contributor remained the FPAR effect (9.6 % $decade^{-1}$, Fig. 7), with intensive use of fertilizers and surface/groundwater irrigation contributing to agricultural intensification. These reasons collectively explain why China and India have led global greening, highlighting the profound impact of human activities on terrestrial ecosystems.

3.4. FPAR effect dominates vegetation carbon fixation divergence across the Amazon region

As previously indicated (Fig. S7), the results consistently show that the Amazon tropical forest regions are experiencing accelerated GPP decline trends (Fig. S9), primarily driven by climate-mediated drought intensification. Both PEM and GOSIF GPP products demonstrated high sensitivity to Amazonian drought and El Niño events, consistently decreasing during occurrences such as 2005, 2010, 2015/2016, and 2023 (Figs. S9–11). While this suggests that the Climate effect dominates the overall regional GPP decline, a spatial analysis (Fig. S12) reveals significant internal variation. By classifying Amazonian vegetation into four productivity ecosystems, a driver analysis (Fig. 8) indicated that the widespread GPP declines caused by the Climate effect (−3.46 % $decade^{-1}$ to −2.75 % $decade^{-1}$) were largely offset by the CFE (2.07 % $decade^{-1}$ to 3.08 % $decade^{-1}$). Crucially, the spatial divergence in GPP trends was primarily driven by the FPAR effect. In the low to moderate productivity ecosystems (5 % area), the FPAR effect was positive (1.54 % $decade^{-1}$ to 2.26 % $decade^{-1}$), leading to a net positive GPP trend (1.69 % $decade^{-1}$ to 3.26 % $decade^{-1}$). Conversely, the high productivity systems (95 % area) exhibited a near-zero or negative FPAR effect (no significant trend to −0.74 % $decade^{-1}$), causing an overall decline in GPP trends (no significant trend to −1.07 % $decade^{-1}$) for these production ecosystems. This pattern means the FPAR effect dominates vegetation carbon fixation divergence across the Amazon, which is likely explained by the light limitation effect in dense, high-productivity ecosystems where increased leaf area primarily creates more shaded leaves (which have lower photosynthetic rates and only utilize diffuse light), while the sunlit leaf area remains unchanged.

4. Discussion

This study analyzed the dynamics and drivers of global vegetation productivity through a data-driven investigation and scenario simulations. Given the substantial impact of simulated GPP uncertainty on the results, we clarify the sources of this uncertainty and outline directions for future improvements. Uncertainties primarily stem from three aspects: (1) FPAR dataset. Our PEM GPP utilized the well-validated SI FPAR as input, which offers higher accuracy than commonly used MODIS & VIIRS FPAR datasets (Pu et al., 2024). For future work, it would be beneficial to complement this with other long-term, high-accuracy FPAR datasets, such as GIMMS FPAR4g (Zhao et al., 2024) and GLASS FPAR (Ma et al., 2022), to generate additional GPP datasets and conduct similar analyses for indirect evaluation. (2) Climate datasets. This study employed two climate datasets, GMAO MERRA-2 and ECMWF ERA-5, to force the PEMs. While using two distinct datasets helps mitigate systematic bias, the upscaling required during GPP generation introduces additional uncertainty. Therefore, incorporating high-resolution climate datasets in future research would further improve GPP quality. (3) Both inherent structural flaws in the PEM models (such as issues with separating sunlit/shaded leaves and light saturation effects) and limitations in the remote sensing input data (specifically the saturation and underestimation of high LAI/FPAR values in dense canopies) collectively lead to the systematic underestimation of GPP when true productivity is high. This significant bias highlights a critical need and large potential for improvement in both canopy photosynthesis modeling and the generation of accurate input data (Jiang et al., 2021). Consequently, developing dynamic LUE_{max} parameters that account for canopy traits (e.g., phenology) could significantly enhance GPP performance. Additionally, creating parametric maps for the environmental factor functions within the three PEMs would also be a valuable advancement.

We acknowledge some limitations regarding the presented sensitivity analysis, particularly in the quantification of the CFE. The first limitation arises from the inherent feedback structure of coupled carbon-climate systems, which, feature intricate linkages involving feedback and lag (Arneth et al., 2010). Although these input-based PEMs used here offer the advantage of simplicity and incorporate measured data (CO_2, climate, and FPAR), they primarily capture only the direct effects of these variables on primary production. Therefore, our sensitivity simulations with PEMs serve primarily to understand the observed spatial patterns of GPP to a first order. The second limitation stems from the mismatch between the scale of modeling and the scale of

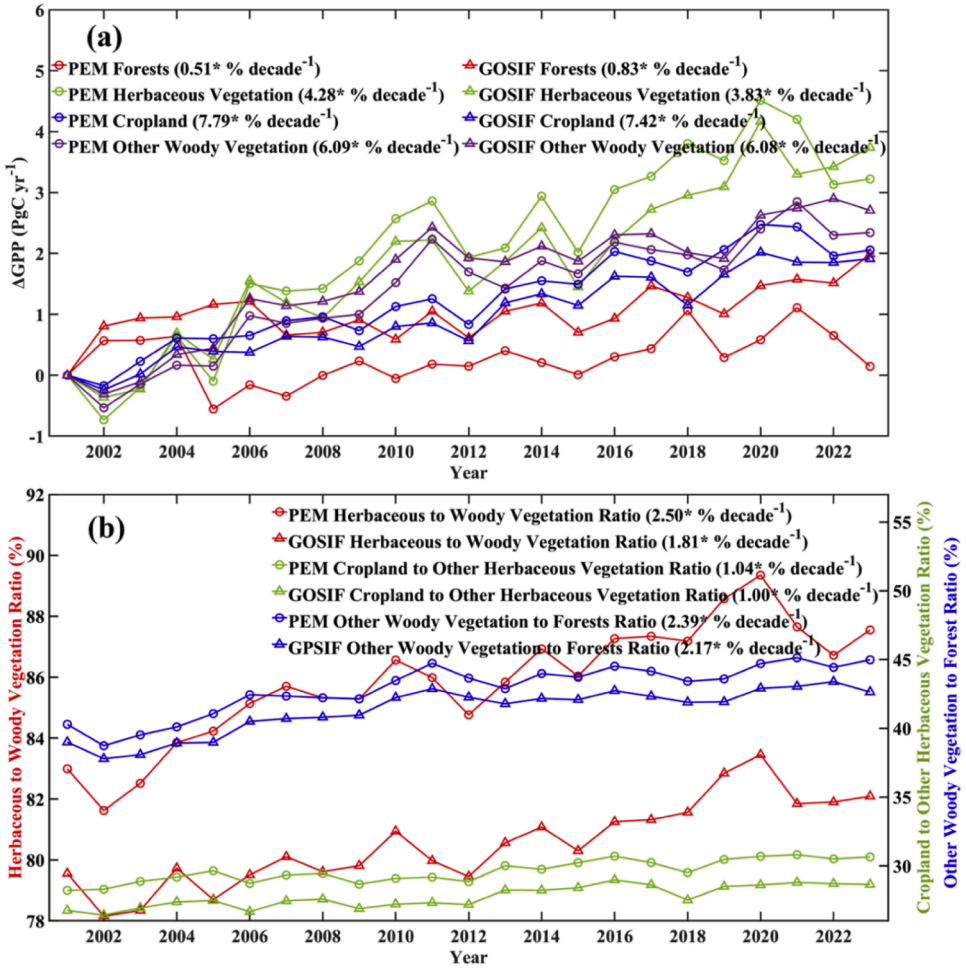

Fig. 4. (a) Dynamics in GPP amongst different vegetation types. (b) Dynamics of GPP ratio of different vegetation types. Forests (red) includes ENF, EBF, DNF, DBF, MF. Herbaceous vegetation (green) includes SAV and GRA. Cropland (blue) includes CRO. Other woody vegetation (purple) includes CSH, OSH, and WSA. Herbaceous to woody vegetation ratio (red) means (Herbaceous vegetation + Croplands) / (Forests + Other woody vegetation). Croplands to other herbaceous vegetation (green) means (Croplands) / (Herbaceous vegetation). Other woody vegetation to forests ration (blue) means (Other woody vegetation) / (Forests).

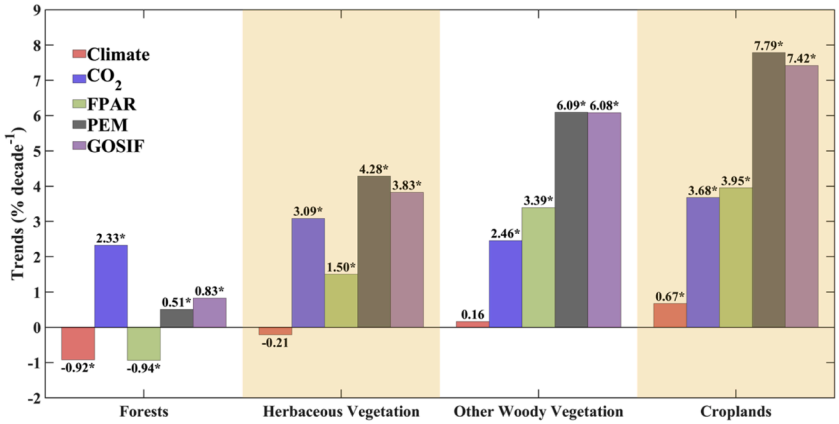

Fig. 5. Trends (PEM and GOSIF GPPs) and drivers (Climate, CO_2, and FPAR effects) for forests, herbaceous vegetation, other woody vegetation, and croplands. Forests include ENF, EBF, DNF, DBF, MF. Herbaceous vegetation includes SAV and GRA. Other woody vegetation includes CSH, OSH, and WSA. Cropland includes CRO.

observation, specifically concerning the CFE. While PEMs define CFE at the leaf scale, remote sensing products, such as FPAR, inherently capture it at the canopy scale (Chen et al., 2022). The process of upscaling from the leaf to the canopy level is complex and cannot be overlooked. Consequently, the CFE quantified in this study is theoretically based on the leaf-scale CO_2 effect within the PEMs, while the actual canopy-scale indirect CFE is implicitly included within the FPAR effect derived from the remote sensing product.

Changes in vegetation structure and leaf area directly alter the light environment within canopies, a phenomenon represented in PEMs

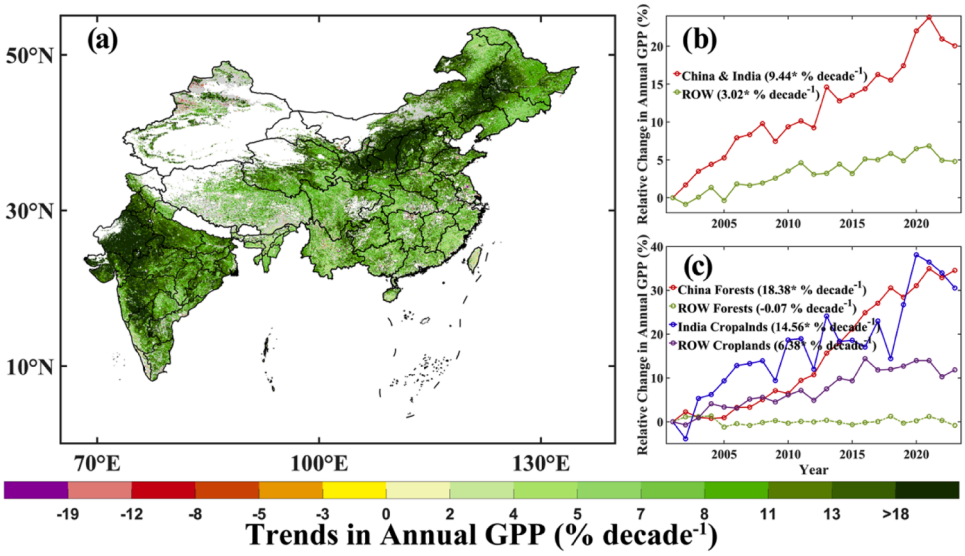

Fig. 6. (a) Trends of PEM GPP production in China & India during 2001–2023. Statistically significant trends (Mann–Kendall test, $P \leq 0.1$) are color-coded. Grey areas show vegetated land with statistically insignificant trends. White areas depict barren lands, permanent ice-covered areas, permanent wetlands, and built-up areas. Blue areas represent water. (b) Photosynthetic production dynamics of China & India (red line) GPP and rest of the world (ROW, green line) during 2001–2023. (c) Photosynthetic production dynamics of China forests (red), ROW forests (green), India croplands (blue), and ROW croplands (purple). '*' means the trend is statistically significant (Mann–Kendall test, $P \leq 0.1$). And dashed line means the trend is not statistically significant (Mann–Kendall test, $P > 0.1$).

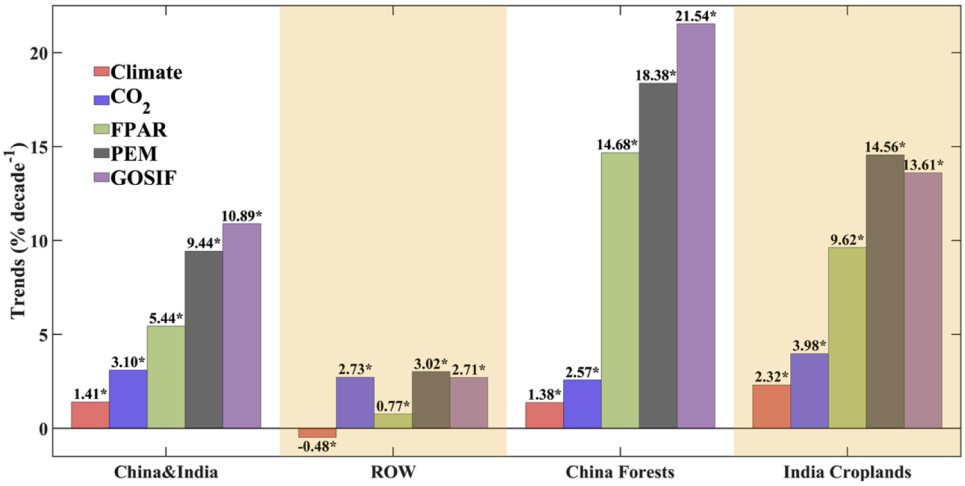

Fig. 7. Same as Fig. 5 but for China & India. Trends (PEM and GOSIF GPPs) and drivers (Climate, CO_2, and FPAR effects) for China & India, Rest of the world (ROW), China forests, and India croplands.

through the FPAR effect. FPAR is a composite diagnostic variable, which captures the integral legacy effects of CO_2 concentration, climate, nutrient availability, and human management on canopy structure (Zhu et al., 2016). While FPAR inherently contains antecedent CO_2/climate-related signals, performing sensitivity analysis on it offers a novel perspective on photosynthesis because it characterizes the proportion of incident light utilized during the light reaction. Focusing on China and India versus the Amazon region, the FPAR effect manifests significantly different roles. Globally, these unique regional outcomes underscore two critical points: (1) the profound importance of human activities, e.g., afforestation in China and agricultural practices in India, for carbon fixation, and (2) the fact that ecosystems with varying productivity levels exhibit divergent trends due to the light limitation effect. In summary, these contrasting regional dynamics highlight that future research and modeling efforts must explicitly focus on the impacts of photosynthetic light reactions, recognizing that these effects stem not only from shifts in CO_2 and climatic conditions but also from the direct influence of human activities.

Several previous studies align with our independent findings: China & India leading global greening: Recent remote sensing-based studies have consistently reported a clear greening trend across Asia, particularly in China and India (Chen et al., 2019a; Piao et al., 2020). Our results corroborate that most parts of China and India exhibit this clear greening pattern, notably in Chinese forests and Indian croplands. This study further quantified the drivers behind this phenomenon through data-based investigation, providing a deeper understanding of how human actions have dominated the greening trends in these two countries. Vegetation response to drought in the Amazon Forest: The Amazon Forest plays an integral role in the global carbon cycle, but increasingly frequent drought events severely disrupt the local terrestrial system (Espinoza et al., 2024). Our results, from the perspective of vegetation carbon fixation, also demonstrated a vulnerability (She et al., 2024) of Amazonian forests to environmental pressures.

This study highlights the critical need to assess whether climate

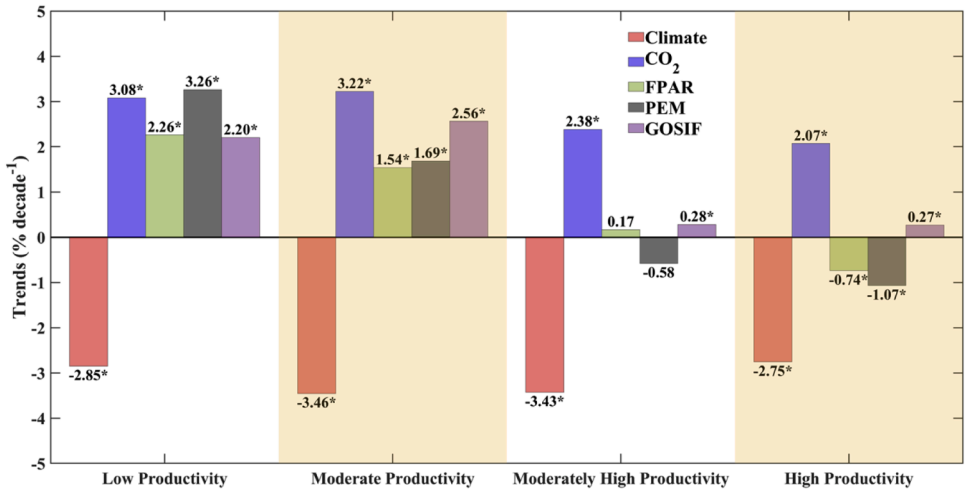

Fig. 8. Same as Fig. 5 but for Amazon forest region. Trends (PEM and GOSIF GPPs) and drivers (Climate, CO_2, and FPAR effects) for 4 different productivity ecosystems in Amazon forest region. The Amazon region covers is a rectangular area spanning 12.5° S to 22.5° N and 83° W to 33° W. Low productivity, Moderate productivity, Moderately High productivity, and High productivity represent annual mean GPP less than 1000 g C m^{-2} yr^{-1}, range within 1000 ~ 2000 g C m^{-2} yr^{-1}, range within 2000 ~ 3000 g C m^{-2} yr^{-1} and greater than 3000 g C m^{-2} yr^{-1}, respectively.

change will emerge as the dominant driver of future vegetation productivity, specifically whether its adverse impacts could negate the CFE (Zhang et al., 2023). While current findings are insufficient for definitive conclusions, preliminary evidence shows regional disparities; for instance, the hypothesis aligns in the Amazon but contradicts in high-latitude Northern Hemisphere regions. To address these uncertainties, future research should leverage CMIP6 (or CMIP7, if available) Earth System Models (ESMs) (Gier et al., 2024) to project climate and CO_2 data. This should be complemented by simulating future FPAR data using methodologies similar to Li et al. (2024) for LAI predictions. By integrating these datasets with PEMs and scenario simulations, researchers could project dynamic trends in GPP and their underlying drivers. Such efforts would advance our understanding of vegetation's capacity to buffer rising atmospheric CO_2 levels and its role in modulating future carbon-climate feedback.

5. Conclusions

Over the past two decades, global vegetation has undergone profound transformations driven by the dual pressures of anthropogenic forcing and climate change. Our newly generated GPP data reveal a notable global greening since the 2000s, with a total increment of almost 10 Pg C yr^{-1}. However, this seemingly positive signal masks complex biogeochemical trade-offs. Based on scenario simulations, this study found that this enhancement has been primarily driven by the continued rise in atmospheric CO_2 concentration, but also significantly influenced by the combined effects of negative climate change and positive human actions. Equally critical are the divergent trends in GPP production among vegetation types: herbaceous vegetation (grasslands, croplands) contributed most to global GPP growth, whereas forests exhibited stagnating productivity under compounding climatic stresses. China and India have achieved remarkable land greening, with afforestation in China and intensive agriculture in India strongly highlighting the positive impacts (positive FPAR effect) of human activities on primary production within ecosystems. The gradual shift of the Amazon Forest from a carbon sink to a source, driven by climate change (intensified drought regimes), but the FPAR effect dominates vegetation carbon fixation divergence across the Amazon region due to the light limitation effect for high productivity ecosystems, which reflects the complexity and vulnerability of tropical forests within the global carbon cycle. These findings underscore the dual role of human activities in shaping ecosystem functioning, while also reminding the scientific community of the importance of strengthening carbon emission management and environmental protection measures to combat climate change and promote the sustainable development of global ecosystems.

Data and code availability

All data used to support the findings of this study are publicly available. The generation code of three PEMs and monthly PEM GPP can be obtained as: https://zenodo.org/records/13989451/.

CRediT authorship contribution statement

Jiabin Pu: Writing – original draft, Visualization, Validation, Software, Methodology, Investigation, Formal analysis, Data curation, Conceptualization. **Si Gao:** Writing – review & editing, Validation, Investigation, Formal analysis. **Kai Yan:** Writing – review & editing, Supervision, Methodology, Investigation. **Xian Sun:** Supervision, Formal analysis. **Alexander J. Winkler:** Writing – review & editing, Resources, Methodology, Conceptualization. **Qiao Wang:** Supervision, Resources. **Ranga B. Myneni:** Supervision, Resources, Project administration, Methodology, Funding acquisition, Conceptualization.

Declaration of competing interest

The authors declare that they have no known competing financial interests or personal relationships that could have appeared to influence the work reported in this paper.

Acknowledgments

The authors thank Nuno Carvalhais at Max-Planck-Institute for Biogeochemistry and Shanning Bao at Chinese Academy of Sciences for help with PEM3. This research was funded by NASA Earth Science Division through MODIS (80NSSC21K1925) and VIIRS (80NSSC21K1960) projects at Boston University.

Supplementary materials

Supplementary material associated with this article can be found, in the online version, at doi:10.1016/j.agrformet.2026.111122.

References

Arneth, A., Harrison, S.P., Zaehle, S., Tsigaridis, K., Menon, S., Bartlein, P.J., Vesala, T., 2010. Terrestrial biogeochemical feedbacks in the climate system. Nat. Geosci. 3 (8), 525–532.

Ballantyne, A., Smith, W., Anderegg, W., Kauppi, P., Sarmiento, J., Tans, P., Running, S., 2017. Accelerating net terrestrial carbon uptake during the warming hiatus due to reduced respiration. Nat. Clim. Chang. 7 (2), 148–152.

Bao, S., Wutzler, T., Koirala, S., Cuntz, M., Ibrom, A., Besnard, S., Carvalhais, N., 2022. Environment-sensitivity functions for gross primary productivity in light use efficiency models. Agric. For. Meteorol. 312, 108708.

Bao, S., Alonso, L., Wang, S., Gensheimer, J., De, R., Carvalhais, N., 2023. Toward robust parameterizations in ecosystem-level photosynthesis models. J. Adv. Model. Earth. Syst. 15 (8) e2022MS003464.

Buck, A.L., 1981. New equations for computing vapor pressure and enhancement factor. J. Appl. Meteorol. Climatol. 20 (12), 1527–1532.

Cai, W., Prentice, I.C., 2020. Recent trends in gross primary production and their drivers: analysis and modelling at flux-site and global scales. Environ. Res. Lett. 15 (12), 124050.

Chen, C., Park, T., Wang, X., Piao, S., Xu, B., Chaturvedi, R.K., Myneni, R.B., 2019a. China and India lead in greening of the world through land-use management. Nat. Sustain. 2 (2), 122–129.

Chen, C., Riley, W.J., Prentice, I.C., Keenan, T.F., 2022. CO2 fertilization of terrestrial photosynthesis inferred from site to global scales. Proc. Natl. Acad. Sci. 119 (10), e2115627119.

Chen, J.M., Ju, W., Ciais, P., Viovy, N., Liu, R., Liu, Y., Lu, X., 2019b. Vegetation structural change since 1981 significantly enhanced the terrestrial carbon sink. Nat. Commun. 10 (1), 4259.

Chen, Y., Zhu, Z., Zhao, W., Li, M., Cao, S., Zheng, Y., Myneni, R.B., 2024a. The direct and indirect effects of the environmental factors on global terrestrial gross primary productivity over the past four decades. Environ. Res. Lett. 19 (1), 014052.

Chen, Z., Wang, W., Forzieri, G., Cescatti, A., 2024b. Transition from positive to negative indirect CO_2 effects on the vegetation carbon uptake. Nat. Commun. 15 (1), 1500.

Cheng, K., Yang, H., Tao, S., Su, Y., Guan, H., Ren, Y., Guo, Q., 2024. Carbon storage through China's planted forest expansion. Nat. Commun. 15 (1), 4106.

Espinoza, J.C., Jimenez, J.C., Marengo, J.A., Schongart, J., Ronchail, J., Lavado-Casimiro, W., Ribeiro, J.V.M., 2024. The new record of drought and warmth in the Amazon in 2023 related to regional and global climatic features. Sci. Rep. 14 (1), 8107.

Farquhar, G.D., von Caemmerer, S.V., Berry, J.A., 1980. A biochemical model of photosynthetic CO2 assimilation in leaves of C3 species. Planta 149 (1), 78–90.

Friedlingstein, P., O'sullivan, M., Jones, M.W., Andrew, R.M., Bakker, D.C., Hauck, J., Zheng, B., 2023. Global carbon budget 2023. Earth. Syst. Sci. Data 15 (12), 5301–5369.

Gao, S., Zhong, R., Yan, K., Ma, X., Chen, X., Pu, J., Myneni, R.B., 2023. Evaluating the saturation effect of vegetation indices in forests using 3D radiative transfer simulations and satellite observations. Remote Sens. Environ. 295, 113665.

Gier, B.K., Schlund, M., Friedlingstein, P., Jones, C.D., Jones, C., Zaehle, S., Eyring, V., 2024. Representation of the terrestrial carbon cycle in CMIP6. Biogeosciences 21 (22), 5321–5360.

Hamed, K.H., Rao, A.R., 1998. A modified Mann-Kendall trend test for autocorrelated data. J. Hydrol. 204 (1–4), 182–196.

Huang, M., Piao, S., Ciais, P., Peñuelas, J., Wang, X., Keenan, T.F., Janssens, I.A., 2019. Air temperature optima of vegetation productivity across global biomes. Nat. Ecol. Evol. 3 (5), 772–779.

Horn, J.E., Schulz, K., 2011. Identification of a general light use efficiency model for gross primary production. Biogeosciences 8 (4), 999–1021.

Jian, D., Niu, G.Y., Ma, Z., Liu, H., Guan, D., Zhou, X., Zhou, J., 2023. Limited driving of elevated CO2 on vegetation greening over global drylands. Environ. Res. Lett. 18 (10), 104024.

Jiang, S., Zhao, L., Liang, C., Cui, N., Gong, D., Wang, Y., Zou, Q., 2021. Comparison of satellite-based models for estimating gross primary productivity in agroecosystems. Agric. For. Meteorol. 297, 108253.

Kalliokoski, T., Mäkelä, A., Fronzek, S., Minunno, F., Peltoniemi, M., 2018. Decomposing sources of uncertainty in climate change projections of boreal forest primary production. Agric. For. Meteorol. 262, 192–205.

Keenan, T.F., Luo, X., Stocker, B.D., De Kauwe, M.G., Medlyn, B.E., Prentice, I.C., Zhou, S., 2023. A constraint on historic growth in global photosynthesis due to rising CO_2. Nat. Clim. Chang. 13 (12), 1376–1381.

Keenan, T.F., Prentice, I.C., Canadell, J.G., Williams, C.A., Wang, H., Raupach, M., Collatz, G.J., 2016. Recent pause in the growth rate of atmospheric CO_2 due to enhanced terrestrial carbon uptake. Nat. Commun. 7 (1), 13428.

Knauer, J., Cuntz, M., Smith, B., Canadell, J.G., Medlyn, B.E., Bennett, A.C., Haverd, V., 2023. Higher global gross primary productivity under future climate with more advanced representations of photosynthesis. Sci. Adv. 9 (46), eadh9444.

Knyazikhin, Y., Martonchik, J.V., Myneni, R.B., Diner, D.J., Running, S.W., 1998. Synergistic algorithm for estimating vegetation canopy leaf area index and fraction of absorbed photosynthetically active radiation from MODIS and MISR data. J. Geophys. Res. Atmosph. 103 (D24), 32257–32275.

Korson, L., Drost-Hansen, W., Millero, F.J., 1969. Viscosity of water at various temperatures. J. Phys. Chem. 73 (1), 34–39.

Krause, A., Papastefanou, P., Gregor, K., Layritz, L.S., Zang, C.S., Buras, A., Rammig, A., 2022. Quantifying the impacts of land cover change on gross primary productivity globally. Sci. Rep. 12 (1), 18398.

Li, X., Xiao, J., 2019. Mapping photosynthesis solely from solar-induced chlorophyll fluorescence: a global, fine-resolution dataset of gross primary production derived from OCO-2. Remote Sens. 11 (21), 2563 (Basel).

Li, H., Zhou, Y., Zhao, X., Zhang, X., Liang, S., 2024. A dataset of 0.05-degree leaf area index in China during 1983–2100 based on deep learning network. Sci. Data 11 (1), 1122.

Li, Y., Ma, X., Yan, K., Cao, C., Zhu, X., Liu, K., 2025. Satellite-observed greening of human-dominated ecosystems in global dryland. J. Remote Sens. 5, 0941.

Liu, Y., Li, Y., Li, S., Motesharrei, S., 2015. Spatial and temporal patterns of global NDVI trends: correlations with climate and human factors. Remote Sens. 7 (10), 13233–13250 (Basel).

Lobell, D.B., Field, C.B., 2008. Estimation of the carbon dioxide (CO_2) fertilization effect using growth rate anomalies of CO_2 and crop yields since 1961. Glob. Chang. Biol. 14 (1), 39–45.

Ma, H., Liang, S., Xiong, C., Wang, Q., Jia, A., 2022. Global land surface 250-m 8-day fraction of absorbed photosynthetically active radiation (FAPAR) product from 2000 to 2020. Earth Syst. Sci. Data 14 (12), 5333–5347.

Mäkelä, A., Pulkkinen, M., Kolari, P., Lagergren, F., Berbigier, P., Lindroth, A., Hari, P., 2008. Developing an empirical model of stand GPP with the LUE approach: analysis of eddy covariance data at five contrasting conifer sites in Europe. Glob. Chang. Biol. 14 (1), 92–108.

Myneni, R.B., Keeling, C.D., Tucker, C.J., Asrar, G., Nemani, R.R., 1997. Increased plant growth in the northern high latitudes from 1981 to 1991. Nature 386 (6626), 698–702.

Nemani, R.R., Keeling, C.D., Hashimoto, H., Jolly, W.M., Piper, S.C., Tucker, C.J., Running, S.W., 2003. Climate-driven increases in global terrestrial net primary production from 1982 to 1999. Science 300 (5625), 1560–1563 (1979).

Novick, K.A., Biederman, J.A., Desai, A.R., Litvak, M.E., Moore, D.J., Scott, R.L., Torn, M. S., 2018. The AmeriFlux network: a coalition of the willing. Agric. For. Meteorol. 249, 444–456.

O'Sullivan, M., Smith, W.K., Sitch, S., Friedlingstein, P., Arora, V.K., Haverd, V., Buermann, W., 2020. Climate-driven variability and trends in plant productivity over recent decades based on three global products. Global. Biogeochem. Cycles 34 (12) e2020GB006613.

Park, T., Gumma, M.K., Wang, W., Panjala, P., Dubey, S.K., Nemani, R.R., 2023. Greening of human-dominated ecosystems in India. Commun. Earth Environ. 4 (1), 419.

Pastorello, G., Trotta, C., Canfora, E., Chu, H., Christianson, D., Cheah, Y.W., Law, B., 2020. The FLUXNET2015 dataset and the ONEFlux processing pipeline for eddy covariance data. Sci. Data 7 (1), 225.

Pei, Y., Dong, J., Zhang, Y., Yuan, W., Doughty, R., Yang, J., Xiao, X., 2022. Evolution of light use efficiency models: improvement, uncertainties, and implications. Agric. For. Meteorol. 317, 108905.

Piao, S., Wang, X., Park, T., Chen, C., Lian, X.U., He, Y., Myneni, R.B., 2020. Characteristics, drivers and feedbacks of global greening. Nat. Rev. Earth Environ. 1 (1), 14–27.

Prentice, I.C., Dong, N., Gleason, S.M., Maire, V., Wright, I.J., 2014. Balancing the costs of carbon gain and water transport: testing a new theoretical framework for plant functional ecology. Ecol. Lett. 17 (1), 82–91.

Prentice, I.C., Balzarolo, M., Bloomfield, K.J., Chen, J.M., Dechant, B., Ghent, D., van Hoolst, R., 2024. Principles for satellite monitoring of vegetation carbon uptake. Nat. Rev. Earth Environ. 5, 818–832.

Pu, J., Yan, K., Roy, S., Zhu, Z., Rautiainen, M., Knyazikhin, Y., Myneni, R.B., 2024. Sensor-independent LAI/FPAR CDR: reconstructing a global sensor-independent climate data record of MODIS and VIIRS LAI/FPAR from 2000 to 2022. Earth Syst. Sci. Data 16 (1), 15–31.

Ruehr, S., Keenan, T.F., Williams, C., Zhou, Y., Lu, X., Bastos, A., Terrer, C., 2023. Evidence and attribution of the enhanced land carbon sink. Nat. Rev. Earth Environ. 4 (8), 518–534.

Running, S.W., & Zhao, M. (2015). Daily GPP and annual NPP (MOD17A2/A3) products NASA Earth Observing System MODIS land algorithm (User's Guide V3).

Sha, Z., Bai, Y., Li, R., Lan, H., Zhang, X., Li, J., Xie, Y., 2022. The global carbon sink potential of terrestrial vegetation can be increased substantially by optimal land management. Commun. Earth Environ. 3 (1), 8.

She, X., Li, Y., Jiao, W., Sun, Y., Ni, X., Zuo, Z., Myneni, R.B., 2024. Varied responses of Amazon forests to the 2005, 2010, and 2015/2016 droughts inferred from multi-source satellite data. Agric. For. Meteorol. 353, 110051.

Sitch, S., O'sullivan, M., Robertson, E., Friedlingstein, P., Albergel, C., Anthoni, P., Zaehle, S., 2024. Trends and drivers of terrestrial sources and sinks of carbon dioxide: an overview of the TRENDY project. Global. Biogeochem. Cycles 38 (7) e2024GB008102.

Smith, W.K., Fox, A.M., MacBean, N., Moore, D.J., Parazoo, N.C., 2020. Constraining estimates of terrestrial carbon uptake: new opportunities using long-term satellite observations and data assimilation. New Phytol. 225 (1), 105–112.

Song, Y., Jiao, W., Wang, J., Wang, L., 2022. Increased global vegetation productivity despite rising atmospheric dryness over the last two decades. Earths Future 10 (7) e2021EF002634.

Stocker, B.D., Wang, H., Smith, N.G., Harrison, S.P., Keenan, T.F., Sandoval, D., Prentice, I.C., 2020. P-model v1. 0: an optimality-based light use efficiency model for simulating ecosystem gross primary production. Geosci. Model. Dev. 13 (3), 1545–1581.

Sulla-Menashe, D., & Friedl, M.A. (2018). User guide to collection 6 MODIS land cover (MCD12Q1 and MCD12C1) product. Usgs: Reston, Va, Usa, 1, 18.

Thornley, J., 2002. Instantaneous canopy photosynthesis: analytical expressions for sun and shade leaves based on exponential light decay down the canopy and an

acclimated non-rectangular hyperbola for leaf photosynthesis. Ann. Bot. 89 (4), 451–458.
Wang, H., Prentice, I.C., Keenan, T.F., Davis, T.W., Wright, I.J., Cornwell, W.K., Peng, C., 2017. Towards a universal model for carbon dioxide uptake by plants. Nat. Plants 3 (9), 734–741.
Wang, S., Zhang, Y., Ju, W., Chen, J.M., Ciais, P., Cescatti, A., Peñuelas, J., 2020. Recent global decline of CO_2 fertilization effects on vegetation photosynthesis. Science 370 (6522), 1295–1300 (1979).
Westermann, S.A., Hildebrandt, A., Bousetta, S., Thober, S., 2024. Does dynamically modeled leaf area improve predictions of land surface water and carbon fluxes? Insights into dynamic vegetation modules. Biogeosciences 21 (22), 5277–5303.
Winkler, A.J., Myneni, R.B., Hannart, A., Sitch, S., Haverd, V., Lombardozzi, D., Brovkin, V., 2021. Slowdown of the greening trend in natural vegetation with further rise in atmospheric CO_2. Biogeosciences 18 (17), 4985–5010.
Yang, Y., Roderick, M.L., Guo, H., Miralles, D.G., Zhang, L., Fatichi, S., Yang, D., 2023. Evapotranspiration on a greening Earth. Nat. Rev. Earth Environ. 4 (9), 626–641.
Yao, Y., Wang, X., Li, Y., Wang, T., Shen, M., Du, M., Piao, S., 2018. Spatiotemporal pattern of gross primary productivity and its covariation with climate in China over the last thirty years. Glob. Chang. Biol. 24 (1), 184–196.
Yuan, W., Liu, S., Zhou, G., Zhou, G., Tieszen, L.L., Baldocchi, D., Wofsy, S.C., 2007. Deriving a light use efficiency model from eddy covariance flux data for predicting daily gross primary production across biomes. Agric. For. Meteorol. 143 (3–4), 189–207.
Zhang, S., Hao, X., Zhao, Z., Zhang, J., Fan, X., Li, X., 2023. Natural vegetation succession under climate change and the combined effects on net primary productivity. Earths Future 11 (11), e2023EF003903.
Zhang, Y., Mao, J., Sun, G., Guo, Q., Atkins, J., Li, W., Hoffman, F., 2025. Earth's record-high greenness and its attributions in 2020. Remote Sens. Environ. 316, 114494.
Zhao, W., Zhu, Z., Cao, S., Li, M., Zha, J., Pu, J., Myneni, R.B., 2024. A global dataset of the fraction of absorbed photosynthetically active radiation for 1982–2022. Sci. Data 11 (1), 707.
Zheng, Y., Shen, R., Wang, Y., Li, X., Liu, S., Liang, S., Yuan, W., 2020. Improved estimate of global gross primary production for reproducing its long-term variation, 1982–2017. Earth Syst. Sci. Data 12 (4), 2725–2746.
Zhu, W., Xie, Z., Zhao, C., Zheng, Z., Qiao, K., Peng, D., Fu, Y.H., 2024. Remote sensing of terrestrial gross primary productivity: a review of advances in theoretical foundation, key parameters and methods. GIsci. Remote Sens. 61 (1), 2318846.
Zhu, Z., Piao, S., Myneni, R.B., Huang, M., Zeng, Z., Canadell, J.G., Zeng, N., 2016. Greening of the Earth and its drivers. Nat. Clim. Chang. 6 (8), 791–795.
Zong, X., Tian, X., Liu, X., Shu, L., 2024. Drought threat to terrestrial gross primary production exacerbated by wildfires. Commun. Earth. Environ. 5 (1), 225.